Journal of Materials Chemistry C

PAPER

View Article Online
View Journal | View Issue

Cite this: J. Mater. Chem. C, 2018, 6, 4967

A high efficiency broad-band near-infrared $Ca_2LuZr_2Al_3O_{12}:Cr^{3+}$ garnet phosphor for blue LED chips

Liangliang Zhang, †*[a] Sheng Zhang, †[ab] Zhendong Hao,[a] Xia Zhang,[a] Guo-hui Pan,[a] Yongshi Luo,[a] Huajun Wu[a] and Jiahua Zhang *[a]

Received 13th March 2018,
Accepted 11th April 2018

DOI: 10.1039/c8tc01216d

rsc.li/materials-c

The garnet $Ca_2LuZr_2Al_3O_{12}$ (CLZA) is a promising broad-band NIR phosphor for blue LED chips when it is doped with Cr^{3+}. The photoelectric efficiency of the pc-LED fabricated from CLZA:Cr^{3+} and a 460 nm LED chip, in the 750–820 nm spectral range, was 4.1%, which was superior to the efficiency of a tungsten lamp (2.9%). In CLZA's structure, Cr^{3+} occupied Ca^{2+}/Lu^{3+} and Zr^{4+} sites and showed two luminescence centers. The crystal strength parameters of Ce^{3+} and Cr^{3+} were calculated to show the coordination environment of the dodecahedral and octahedral sites in CLZA. Low absorbance of Cr^{3+} was the main constraint on quantum efficiency. Ce^{3+} was thus introduced as a sensitizer to improve the absorbance. An efficient energy transfer process can be observed between Ce^{3+} and Cr^{3+} in CLZA. The temperature dependent properties of CLZA:Cr^{3+} were also studied. Two thermal processes (thermal quenching and thermal ionization) were observed and discussed in detail.

Introduction

As they are now required in new applications like the non-destructive measuring of the quality attributes of agricultural products[1,2] and the noninvasive monitoring of human physiological states,[3,4] broad-band near infrared (NIR) light sources have received increasing interest.[5,6] When NIR radiation passes through biological tissue, the light may be reflected or absorbed by some kind of substance.[7] The reflected or transmitted NIR light is measured to show any changes to the NIR spectrum.[8] This will provide information such as the sugar content of vegetables, internal damage in fruits, blood oxygenation in human arteries,[9,10] *etc.* Among these applications, a broad-band NIR light source for high depth resolution is needed.[11] NIR light emitting diodes (LEDs) are common NIR light sources. However, the emission bands of NIR LEDs are narrow (<50 nm).[12] This is insufficient for most spectroscopic applications. The tungsten lamp is a traditional light source with very broad NIR emission. However, the tungsten lamp has a short lifetime and low efficiency, and is large in size.[13] An ideal broad-band near infrared (NIR) light source is still needed. Thus, people have tried to develop NIR phosphors that can combine with blue LED chips to construct phosphor converted LED (pc-LED) devices. The NIR pc-LED follows the same principle as white LEDs (WLEDs) and has been proven to have a long lifetime and high efficiency, to be cheap, and to be small in size.[14] The existing problem is to develop an efficient broad-band NIR phosphor that matches well with blue LED chips.

Trivalent rare-earth (RE^{3+}) ions are some of the most studied luminescence centers for broad-band NIR emission. A Pr^{3+} doped Bi_2O_3–Sb_2O_3–B_2O_3 glass phosphor realized a 0.25 mW output power when excited by a 470 nm LED chip with an injection current of 1000 mA.[15] A Yb^{3+} and Nd^{3+} co-doped Bi_2O_3–B_2O_3 glass phosphor showed a 1 mW output power when combined with a 590 nm LED with an 815 mA current.[16] The luminescence efficiencies of Tm^{3+} doped Sb_2O_3–ZnO–GeO_2–B_2O_3 glass phosphors around 800 nm were 0.02–0.20%.[17] The quantum efficiency (QE) of a Eu^{2+}, Nd^{3+} co-doped $Sr_2Si_5N_8$ NIR phosphor for blue LED chips at the NIR region reached 26%.[18] However, the bandwidth was narrow. Research has also focused on transition metal ions to realize broad NIR emission. For example, Ni^{2+} doped lithium-alumina-silicate glass-ceramics showed emission around 1300 nm with a full-width at half maximum (FWHM) of 342 nm.[19] Ni^{2+} doped $ZnGa_2O_4$ showed emission from 1100 nm to 1700 nm with a FWHM of 288 nm.[20] V^{3+} doped gallium lanthanum sulphide glass (V:GLS) showed emission at 1500 nm with a FWHM of 500 nm.[21] The QE of V:GLS was 4%. Akvile *et al.* reported Cr^{3+} doped $Gd_3Ga_5O_{12}$ (GGG), $Y_3Ga_5O_{12}$ (YGG), $Lu_3Ga_5O_{12}$ (LGG), and $Gd_3Sc_2Ga_3O_{12}$ (GSGG) garnet phosphors. The emission of these phosphors

[a] State Key Laboratory of Luminescence and Applications, Changchun Institute of Optics, Fine Mechanics and Physics, Chinese Academy of Sciences, 3888 Eastern South Lake Road, Changchun 130033, China. E-mail: zhangliangliang@ciomp.ac.cn, zhangjh@ciomp.ac.cn
[b] University of Chinese Academy of Sciences, Beijing, 100049, China
† These authors contributed equally to this work.

ranged from 705 nm to 759 nm.[22] The internal QE of the optimized phosphors was 46% when excited at 445 nm. Among these NIR phosphors, Cr^{3+} showed higher efficiency and matched well with blue LED chips. However, the bandwidth of Cr^{3+} was narrower and the emission wavelength was shorter.

There are two possible luminescence levels in Cr^{3+}: ^2E_g and $^4T_{2g}$.[23] The emission from ^2E_g is sharp (spin forbidden) and the emission from $^4T_{2g}$ is broad (spin allowed).[24] The position of $^4T_{2g}$ is controlled by the crystal field strength of the ligating atoms.[25] A weak crystal field environment is necessary for broad and efficient emission of Cr^{3+}. Since Cr^{3+} has an octahedral geometry with six O atoms, a larger center ion causes a weak field.[26] Ions like Ga^{3+}, Sc^{3+} *etc.* are considered to be good centers for broad Cr^{3+} emission. In the substation process, the valence is unchanged. However, placing Cr^{3+} in a non-trivalent site introduces more disturbance to the electron orbit of Cr^{3+}. This may inspire new luminescence properties. Furthermore, the luminescence of Cr^{3+} in smaller dodecahedral (Ca^{2+}) and larger tetrahedral (Ge^{4+}) sites was also reported in garnet structures recently.[27] This challenges the conventional picture of Cr^{3+} luminescence that could only be observed in octahedral sites, and provides a new breakthrough to realize a broader emission band of Cr^{3+}.

Garnet is an ideal host material for Cr^{3+}. The chemical formula of garnet is summarized as $A_3C_2D_3O_{12}$. The A site has dodecahedral coordination, the C site has octahedral coordination, and the D site has tetrahedral coordination. In this paper, we doped Cr^{3+} into a $Ca_2RZr_2Al_3O_{12}$ (R = Lu, Y, Gd) garnet. The structure consists of Ca^{2+}/Lu^{3+} dodecahedral sites and Zr^{4+} octahedral sites. These sites are charge-imbalanced and large in volume for Cr^{3+}. These properties promise Cr^{3+} to show higher efficiency and broader emission band in $Ca_2RZr_2Al_3O_{12}$ garnet.

Experimental section

Synthesis

Ce^{3+} doped, Cr^{3+} doped and Ce^{3+}, Cr^{3+} co-doped CLZA, CYZA, and CGZA phosphors were synthesized *via* the traditional solid state method. $CaCO_3$ (99.99%), Lu_2O_3 (99.9%), Y_2O_3 (99.9%), Gd_2O_3 (99.9%), ZrO_2 (99.99%), Al_2O_3 (99.9%), Cr_2O_3 (99.99%), and CeO_2 (99.99%) were used as raw materials. The materials were weighed and ground in an agate mortar for 30 minutes. Then, the mixtures were transferred into an alundum crucible and put into a tube furnace. The heating rate was 3 °C min^{-1}. The temperature was firstly maintained at 900 °C for 1 h and then raised to 1600 °C. The samples were protected using a 5% H_2/N_2 gas flow throughout the whole sintering process.

Characterization

X-ray powder diffraction (XRD) patterns were obtained on a D8 Focus diffractometer (Cu Kα, 40 kV, 40 mA, Bruker, Germany). The diffractometer was equipped with a LYNXEYE 1-dimensional detector to realize very quick measurement. The XRD data were obtained in the range of 25°–70° with a step size of 0.02° and a count time of 3 s per step. The Rietveld refinement was performed using the FullProf program.

The excitation and emission spectra were recorded using an F-7000 spectrometer (HITACHI, Japan) with a 200 W Xe lamp. The excitation and emission slits were both set at 5 nm. The quantum efficiency (QE) was also recorded using the F-7000 spectrometer with an additional integrating sphere fitting. $BaSO_4$ was used for calibration. The decay curves were recorded using an FL920 spectrometer (Edinburgh Instruments, UK) with a hydrogen lamp (nF900). The pulse time of the light source was 1 ns. Diffuse reflection (DR) spectra were recorded using a UV-3600plus UV-VIS-NIR spectrometer (Shimadzu, Japan). An integrating sphere system was equipped for powder DR measurement. $BaSO_4$ powder was used for calibration. All of the above measurements were processed at room temperature (RT).

The temperature dependent properties were measured using a BX53M fluorescence microscopy system (Olympus, Japan). The system was equipped with a U-HGLGPS light source (Short arc mercury lamp, 130 W, Olympus, Japan), a THMS600E cooling–heating platform (77–873 K, Linkam Scientific Instruments, UK), and a QEPro micro fiber spectrometer (200–1000 nm, Ocean Optics, USA). The photoelectric properties of the pc-LEDs and tungsten lamp were measured using a HAAS 2000 photoelectric measuring system (350–1100 nm, EVERFINE, China). The forward bias current for pc-LEDs was 20 mA.

Results and discussion

Phase identification

The phases of the Ce^{3+} and Cr^{3+} doped CLZA phosphors were examined using XRD, as shown in Fig. 1. Most of the diffraction peaks were indexed to the CLZA phase except for the one at 30.15°. This is the characteristic peak of the ZrO_2 raw material. ZrO_2 is very stable with a melting point of 2700 °C. Thus, ZrO_2 is inactive and doesn't react completely in the sintering process. The CLZA structure evolved from the $Lu_3Al_5O_{12}$ (LuAG) garnet with two Ca^{2+}–Zr^{4+} substituting for Lu^{3+}–Al^{3+}. However, the radius of Ca^{2+} is larger than that of Lu^{3+} and the radius of Zr^{4+} is larger than that of Al^{3+}. The lattice of CLZA is expected to be expanded compared to that of LuAG. The impurity ZrO_2 phase belongs to the $Fm\bar{3}m$ space group with JCPDF number 49-1642. Since the luminescence of Ce^{3+} and Cr^{3+} is not reported in ZrO_2, we ignored the influence of the ZrO_2 impurity on the emission positions of Ce^{3+} and Cr^{3+} in CLZA. However, the efficiency of the CLZA phosphors involved in this paper can be further improved by removing these ZrO_2 impurities. To understand the detailed ion substitution processes in CLZA, Rietveld refinement was performed with LuAG as the initial model. Fig. 2 shows the plot of the Rietveld refinement results. ZrO_2 is introduced as the second phase in the Rietveld refinement. The weight fraction of ZrO_2 suggested by the refinement was only 1.81 wt%. The values of the residual factors were R_{wp} = 5.55%, R_p = 4.42%, and χ^2 = 3.3. The cell parameters were $a = b = c$ = 12.3994 Å, as shown in Table 1. The atomic parameters of CLZA are shown in Table 2. Ca^{2+} ions occupy

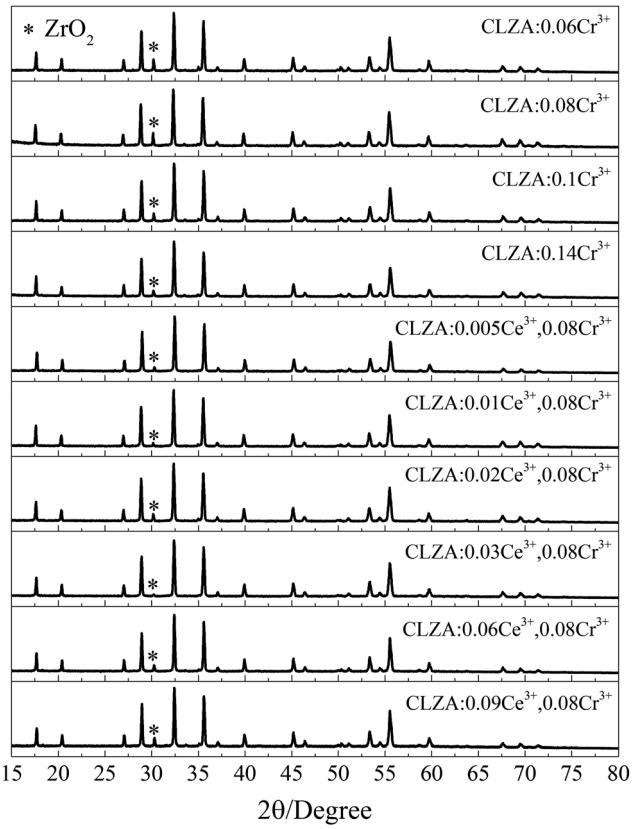

Fig. 1 X-ray powder diffraction patterns of Ce^{3+} and Cr^{3+} doped CLZA.

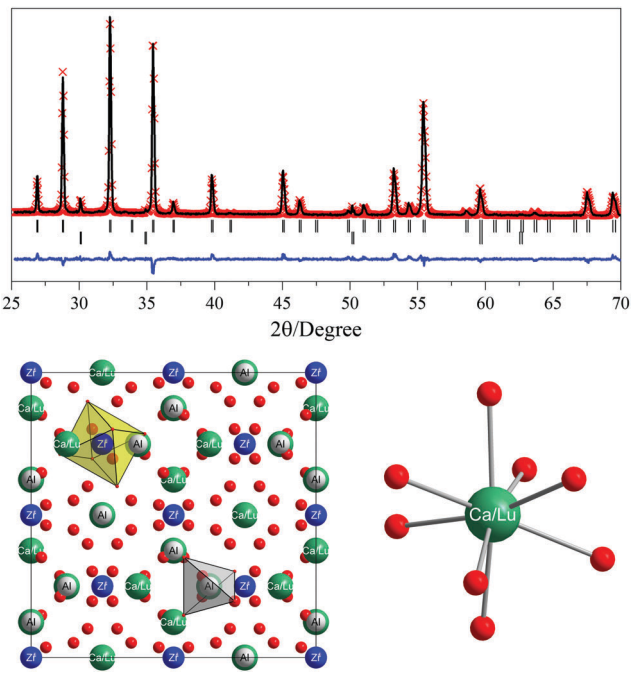

Fig. 2 Rietveld refinement X-ray diffraction of CLZA and the crystal structure of CLZA.

the same sites as the Lu^{3+} ions. Zr^{4+} ions occupy the octahedral sites of the garnet structure.

Table 1 Crystallographic data for CLZA

Formula	$Ca_2LuZr_2Al_3O_{12}$
Crystal system	Cubic
Space group	$Ia\bar{3}d$
Lattice parameters	
$a = b = c$ (Å)	12.3994
$\alpha = \beta = \gamma$ (°)	90
Cell volume (Å^3)	1906.3

Table 2 Atomic parameters of CLZA

Atom	Wyck.	x	y	z	SOF
Ca	24c	1/8	0	0	0.6667
Lu	24c	1/8	0	0	0.3333
Zr	16a	0	0	0	1
Al	24d	1/8	0	3/4	1
O	96h	0.0357	0.0518	0.6487	1

Fig. 2 shows the crystal structure of CLZA and the local coordination of the Ca^{2+}/Lu^{3+}, Zr^{4+} and Al^{3+} sites. The coordination number of Ca^{2+}/Lu^{3+} was 8. Ce^{3+} entered this site because of its similar radius and charge. The average Ca/Lu–O distance was 2.4779 Å. Zr^{4+} formed a [ZrO6] octahedron. The average Zr–O distance was 2.002 Å. Cr^{3+} luminescence generally originated from this site. Al^{3+} formed an [AlO4] tetrahedron and Cr^{3+} showed no luminescence when entering this site. The average Al–O distance was 1.7934 Å.

Luminescence properties

Fig. 3 shows the excitation and emission spectra of CLZA:0.08Cr^{3+}. Cr^{3+} exhibited a large absorption range from UV to red. The excitation bands can be divided into three parts: 200–350 nm, 350–550 nm and 550–750 nm. The excitation at 350–550 nm originated from the transition between $^4A_{2g}$ and $^4T_{1g}$. The excitation at 550–750 nm originated from the transition between $^4A_{2g}$ and $^4T_{2g}$. A sharp shoulder peak at 692 nm (R-lines) originated from the transition between $^4A_{2g}$ and ^2E_g. Cr^{3+} showed a broad emission from 650 nm to 850 nm in CLZA. This band originated from the $^4T_{2g} \rightarrow {}^4A_{2g}$ transition of Cr^{3+}. A little bump of the emission band at 692 nm should be noted. This originated from the $^2E_g \rightarrow {}^4A_{2g}$ transition. Normally, a broad emission band can be observed only when Cr^{3+} occupies a site with a weak crystal field. In summary, CLZA:Cr^{3+} phosphor matches well with 460 nm

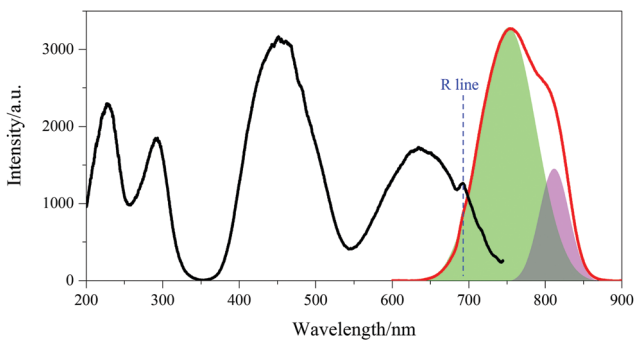

Fig. 3 Excitation and emission spectra of CLZA:0.08Cr^{3+}.

blue LED chips and emits a broad-band in the NIR region. Thus CLZA:Cr^{3+} is a promising NIR phosphor.

The emission band of CLZA:0.08Cr^{3+} can be divided into two sub-bands centered at 754 nm and 813 nm respectively. This indicates the two Cr^{3+} centers in CLZA. The band centering at 754 nm is called Cr1 and the other band is called Cr2 in this paper. There are three possible sites for Cr^{3+} in CLZA: the dodecahedral Ca^{2+}/Lu^{3+} site, the octahedral Zr^{4+} site, and the tetrahedral Al^{3+} site. To our knowledge, luminescence of Cr^{3+} in the tetrahedral Al^{3+} site hasn't been reported. Thus we considered Cr^{3+} to occupy the Zr^{4+} and Ca^{2+}/Lu^{3+} sites. The luminescence of Cr^{3+} in the garnet structure always originates from the octahedral sites. Luminescence of Cr^{3+} in the dodecahedral site is unusual. Also, the broad emission of the Cr^{3+} in the Ca^{2+}/Lu^{3+} sites suggests a weak crystal field. However, the dodecahedral sites in the garnet structure are always considered to have a strong crystal field.

Ce^{3+} occupies the dodecahedral sites in the garnet structure. Ce^{3+} can be used as a probe to show the relative strength of the crystal field. Two parameters are introduced to describe the crystal field: the centroid shift (ε_c) and the crystal field splitting (ε_{cfs}) of the Ce^{3+} 5d levels. ε_c relates to the covalence of the ligand atoms, and ε_{cfs} relates to the ionicity between the center and ligand atoms. In this paper, we used the method proposed by P. Dorenbos to estimate ε_c and ε_{cfs}.[28–30] Table 3 shows the summary of the ε_c and ε_{cfs} values of Ce^{3+} in different compounds. YAG is a well-known compound with a strong crystal field strength. Compared to YAG, the ε_c values of CLZA, CYZA, and CGZA were much larger while the ε_{cfs} values were much smaller. Surprisingly, the ε_c and ε_{cfs} values of CLZA, CYZA, and CGZA were similar to those of $CaSiN_2$. $CaSiN_2$ is a nitride compound with a high covalence and a low crystal field strength. This proves that the crystal field strength of the dodecahedral $Ca^{2+}/Lu^{3+}/Y^{3+}/Gd^{3+}$ sites in CLZA, CYZA, and CGZA was very weak.

D_q and B are important crystal field parameters of Cr^{3+}. $10D_q$ is the energy gap between the e_g and t_{2g} orbitals in the octahedral sites. B is the Racah inter-electronic repulsion parameter. The ratio of D_q/B represents the strength of the crystal field. A smaller D_q/B indicates a weaker crystal field. Henry, Tanabe and Sugano developed a method to calculate D_q and B:[35]

$$\begin{aligned} 10 \cdot D_q &= E_a\left({}^4T_{2g}\right) \\ D_q/B &= \frac{15 \cdot (x-8)}{x^2 - 10 \cdot x} \\ D_q \cdot x &= E_a\left({}^4T_{1g}\right) - E_a\left({}^4T_{2g}\right) \end{aligned} \quad (1)$$

$E_a({}^4T_{1g})$ and $E_a({}^4T_{2g})$ are the equilibrium positions of the ${}^4T_{1g}$ and ${}^4T_{2g}$ levels given by the peaks of the absorption bands.

Table 3 Centroid shift and crystal field splitting of the Ce^{3+} 5d levels in different materials

	5d excitation bands (nm)	ε_c (cm^{-1})	ε_{cfs} (cm^{-1})	Ref.
$Y_3Al_5O_{12}$	205, 225, 261, 340, 458	14 700	27 000	31
$Ca_2LuZr_2Al_3O_{12}$	333, 351, 384, 395, 410	24 380	5640	This work
$Ca_2YZr_2Al_3O_{12}$	340, 390, 415	27 134	5315	32
$Ca_2GdZr_2Al_3O_{12}$	—	24 580	5345	33
$CaSiN_2$	365, 390, 440, 535	27 616	8706	34

Table 4 Crystal field parameters of Cr^{3+} in different garnet sites

	CLZA:Cr1	CLZA:Cr2	$(La,Lu)_5Ga_3O_{12}$ (LLGG:Cr^{3+})	$Y_3Ga_5O_{12}$ (YGG:Cr^{3+})
$E_a({}^4T_{2g})$ (cm^{-1})	15 161	15 755	14 800	16 300
$E_a({}^4T_{1g})$ (cm^{-1})	22 435	22 281	20 920	22 730
D_q (cm^{-1})	1516	1576	1480	1630
B (cm^{-1})	790	646	619	639
D_q/B (cm^{-1})	1.92	2.38	2.39	2.55
Emission (cm^{-1})	13 297	12 269	~12 000	~13 500
Ref.	This work	This work	35	35

Table 4 summarises the D_q and B values in CLZA, LLGG and YGG. One can see that the D_q/B value of Cr2 equalled 2.38, which was similar to that of LLGG:Cr^{3+} (2.39) but smaller than that of YGG:Cr^{3+} (2.55). Correspondingly, the emission wavelength of Cr2 was also similar to that of LLGG:Cr^{3+} and longer than that of YGG:Cr^{3+}. The D_q/B value of Cr2 was in accord with the luminescence behaviour of Cr^{3+} in the octahedral sites of garnet. Thus, Cr2 was considered to have occupied the Zr^{4+} sites in CLZA. On the other hand, the luminescence behaviour of Cr1 was obviously different. The D_q/B value of Cr1 equalled 1.92, which was much smaller than that of YGG:Cr^{3+} and that of LLGG:Cr^{3+}. However, the emission wavelength of Cr1 was shorter than that of LLGG:Cr^{3+} and similar to that of YGG:Cr^{3+}. Thus, Cr1 should have originated from the Ca^{2+}/Lu^{3+} sites of CLZA.

Fig. 4a shows the emission spectra of Cr^{3+} in CLZA, CYZA, and CGZA. The emission peaks of Cr^{3+} show an obvious redshift. The relative emission intensity of Cr2 also increased. This can be

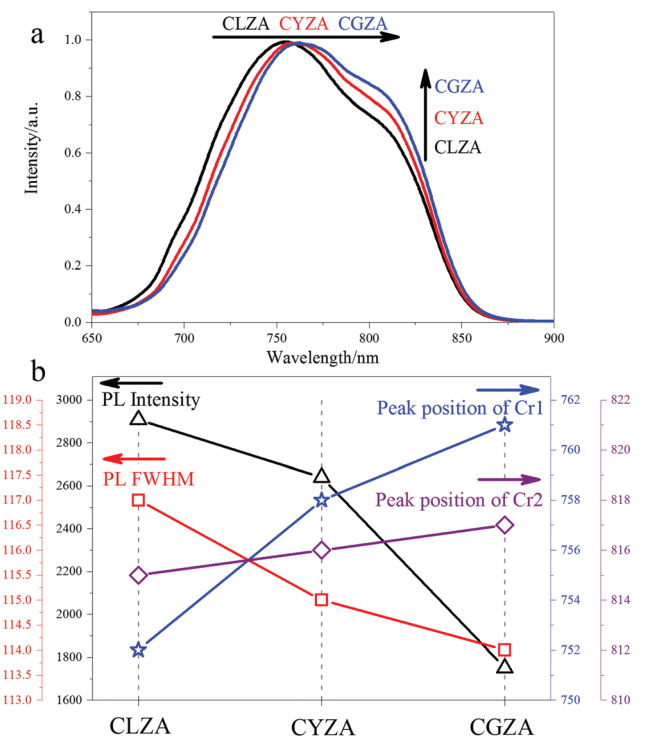

Fig. 4 (a) Emission spectra of Cr^{3+} in CLZA, CYZA and CGZA. (b) Emission intensity of Cr^{3+}, FWHM of Cr^{3+}, and peak position of Cr1 and Cr2 in CLZA, CYZA, CGZA.

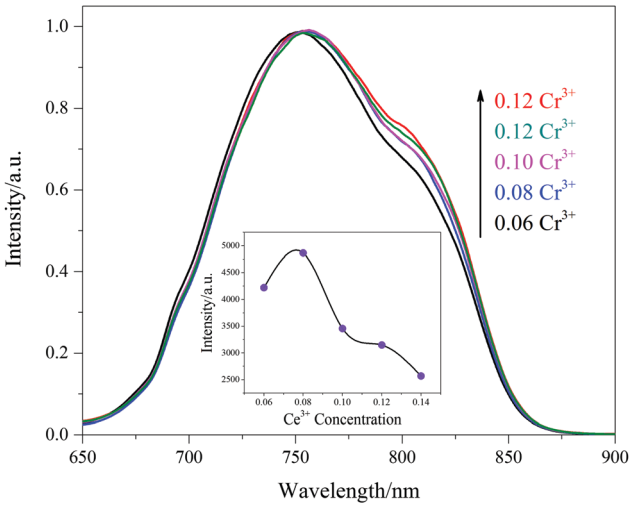

Fig. 5 Normalized emission spectra of CLZA with different Cr^{3+} concentrations.

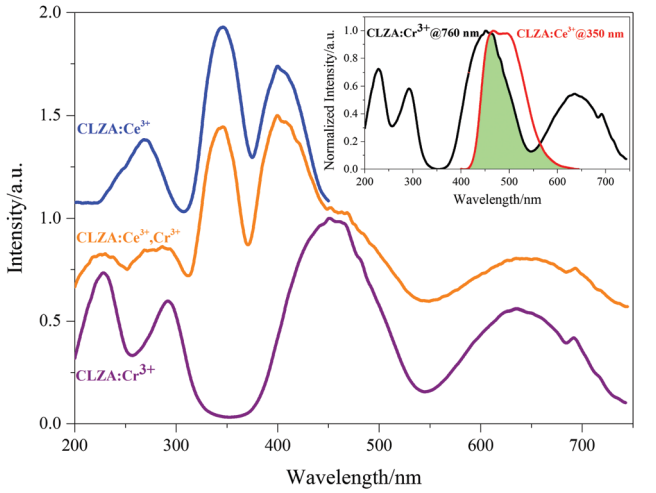

Fig. 6 Excitation spectra of CLZA:Ce^{3+} monitoring at 470 nm, CLZA:Ce^{3+},Cr^{3+} monitoring at 760 nm and CLZA:Cr^{3+} monitoring at 760 nm. The inset shows the overlap between the excitation spectrum of CLZA:Cr^{3+} (760 nm) and the emission spectrum of CLZA:Ce^{3+} (350 nm).

explained by the crystal field effect. The radius of Lu^{3+} is 0.977 Å, the radius of Y^{3+} is 1.019 Å, and the radius of Gd^{3+} is 1.053 Å. A bigger radius results in a weaker crystal field. Thus, Cr^{3+} emission shows a redshift. Cr1 occupied the Ca^{2+}/Lu^{3+}/Y^{3+}/Gd^{3+} sites, and the redshift of Cr1 should be bigger than Cr2, as shown in Fig. 4b. The order of the radii was Cr^{3+} < Lu^{3+} < Y^{3+} < Gd^{3+}. The larger the radius difference was, the more difficult it was for Cr^{3+} to enter the site. The probability of Cr^{3+} entering Zr^{4+} sites was, on the contrary, increased in the order CLZA, CYZA, and CGZA. Thus, the emission intensity of Cr2 increased. Fig. 4b shows the emission intensity and FWHM of Cr^{3+} in CLZA, CYZA, and CGZA. CLZA:Cr^{3+} showed the highest intensity and the broadest emission band.

Fig. 5 shows the normalized emission spectra of the CLZA:$x$$Cr^{3+}$ samples. With increasing Cr^{3+} concentration, the relative emission intensity of Cr2 increased. This indicates that Cr^{3+} preferentially entered the Zr^{4+} sites at higher concentration. The emission wavelength of CLZA:Cr^{3+} shows a little redshift with increasing Cr^{3+} concentration. Since the radius of Cr^{3+} is smaller than that of Lu^{3+}, the redshift wasn't caused by a change in the crystal field. It may have been caused by energy migration between the Cr^{3+} ions.[36] The energy of an excited Cr^{3+} ion may migrate to nearby Cr^{3+} ions with lower $^4T_{2g}$ levels. The optimal Cr^{3+} concentration was 0.08, and a higher Cr^{3+} concentration resulted in concentration quenching.

Energy transfer

Absorption of Cr^{3+} is weak. This is an inherent property of Cr^{3+} caused by the transition inside the 3d orbit. One solution to this problem is to introduce a sensitizer with a strong absorption ability. In this paper, Ce^{3+} was introduced as a sensitizer. Ce^{3+} always shows strong absorption with a transition between the 4f–5d orbits. Emission of Ce^{3+} in CLZA shows a broad band centered at 470 nm. As shown in the inset picture in Fig. 6, emission of Ce^{3+} shows a large overlap with the excitation spectrum of Cr^{3+}. This implies that there is an efficient energy transfer between Ce^{3+} and Cr^{3+}. Fig. 6 shows the excitation spectra of Ce^{3+}-doped, Cr^{3+}-doped and Ce^{3+},Cr^{3+} co-doped CLZA. The excitation spectrum of CLZA:Ce^{3+},Cr^{3+} monitoring Cr^{3+} emission consists of the characteristic excitation peaks of Ce^{3+} at 350 nm and 410 nm. This confirms the energy transfer from Ce^{3+} to Cr^{3+}. In the excitation spectrum of CLZA:Ce^{3+},Cr^{3+}, the excitation intensity of the peaks originating from Ce^{3+} is even stronger than that of Cr^{3+} itself. Ce^{3+} was an effective sensitizer for Cr^{3+} in CLZA.

Fig. 7 shows the decay curves of CLZA:0.03Ce^{3+},$y$$Cr^{3+}$ monitoring at 470 nm. The decay of CLZA:0.03Ce^{3+} showed an ideal single exponential process. When Cr^{3+} was introduced, the decay was accelerated and changed into a non-single exponential process. This was caused by the energy transfer process from Ce^{3+} to Cr^{3+}. The energy transfer rate (η) was 74.73%, 75.43%, 81.49%, and 84.11% for y = 0.06, 0.08, 0.10, and 0.12, respectively, as

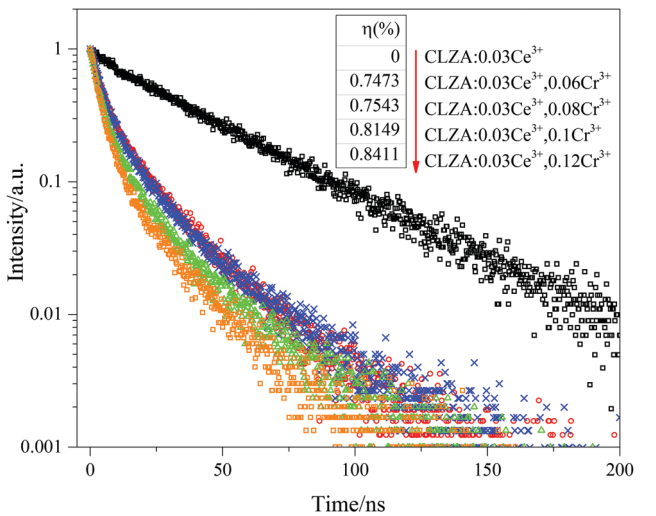

Fig. 7 Decay curves of CLZA:0.03Ce^{3+},$y$$Cr^{3+}$ with different Cr^{3+} concentrations monitoring at 470 nm (excited by 350 nm).

shown in Fig. 7. The energy transfer rate was high and suggests an efficient energy transfer from Ce^{3+} to Cr^{3+}.

The decay curves of CLZA:0.03Ce^{3+},yCr^{3+} can be expressed using the Inokuti–Hirayama formula:

$$I(t) = I_0(t) \times \exp\left[-\frac{4}{3}\pi\Gamma\left(1-\frac{3}{s}\right)N_a\alpha^{3/s}t^{3/s}\right] \quad (2)$$

where $I(t)$ represents the decay curve of Ce^{3+}. $I_0(t)$ represents the decay curve of Ce^{3+} without Cr^{3+}. s is a coefficient with a value of 6, 8, and 10 for dipole–dipole, dipole–quadrupole, and quadrupole–quadrupole interactions, respectively. N_a is the number of acceptors per unit volume. It can be derived that $\log\{-\ln[I_d/I_0]\}$ shows a linear dependence on $\log(t)$ with a slope of $3/s$. As shown in Fig. 8a, the s values equal 7.2, 7.8, and 7.9 for y = 0.08, 0.10, and 0.12, respectively. This indicates that the electronic interaction type of the $Ce^{3+} \rightarrow Cr^{3+}$ transfer was dipole–quadrupole. This is different from the $Ce^{3+} \rightarrow Cr^{3+}$ energy transfer process in YAG as that is a dipole–dipole interaction.[37]

The critical energy transfer distance R_0 is the distance between the donor–acceptor pair where the energy transfer rate is the same as the spontaneous radiation rate. R_0 can be calculated using the equation: $R_0^8 = \alpha \times \tau_0$. α is a rate constant for energy transfer and can be calculated through a transformed Inokuti–Hirayama formula:

$$\ln\frac{I(t)}{I_0(t)} = -\frac{4}{3}\pi\Gamma\left(\frac{1}{2}\right)n_A\alpha^{3/8}t^{3/8} \quad (3)$$

As shown in Fig. 8b, α for the $Ce^{3+} \rightarrow Cr^{3+}$ transfer in CLZA:0.03Ce^{3+},0.08Cr^{3+}, CLZA:0.03Ce^{3+},0.1Cr^{3+}, and CLZA:0.03Ce^{3+},0.12Cr^{3+} equalled 0.961×10^{-50} cm^8 s^{-1}, 1.363×10^{-50} cm^8 s^{-1}, and 2.032×10^{-50} cm^8 s^{-1} respectively. τ_0 for the $Ce^{3+} \rightarrow Cr^{3+}$ energy transfer was 37.604 ns, which was obtained by integrating the decay curve of CLZA:0.03Ce^{3+}. R_0 is calculated to be 6.603 Å, 6.898 Å and 7.251 Å for CLZA:0.03Ce^{3+},0.08Cr^{3+}, CLZA:0.03Ce^{3+},0.1Cr^{3+}, and CLZA:0.03Ce^{3+},0.12Cr^{3+}, respectively.

The critical concentration C_0 is the concentration when the energy transfer rate is equal to the spontaneous radiation rate.

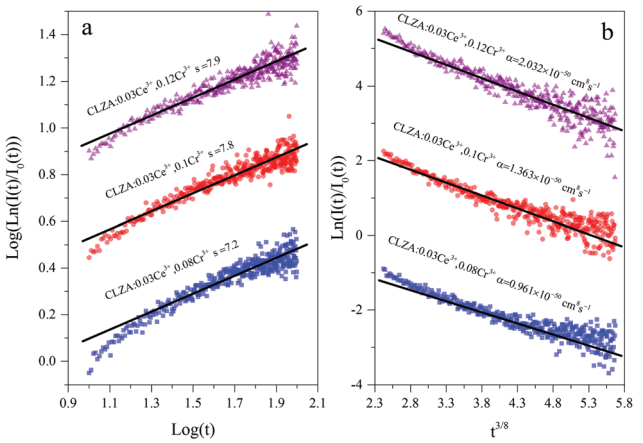

Fig. 8 (a) Relationship between $\log[-\ln(I(t)/I_0(t))]$ and $\log(t)$ of CLZA:0.03-Ce^{3+},yCr^{3+}. (b) Plot of $\ln[I(t)/I_0(t)]$ *vs.* $t^{3/8}$ for sample CLZA:0.03Ce^{3+},yCr^{3+}.

Table 5 Energy transfer parameters for CLZA:0.03Ce^{3+},yCr^{3+} samples

Sample	Calculated s	α (cm^8 s^{-1})	R_0 (Å)	C_0
CLZA:0.03Ce^{3+},0.08Cr^{3+}	7.2	0.961×10^{-50}	6.603	0.066
CLZA:0.03Ce^{3+},0.1Cr^{3+}	7.8	1.363×10^{-50}	6.898	0.058
CLZA:0.03Ce^{3+},0.12Cr^{3+}	7.9	2.032×10^{-50}	7.251	0.050
Average value	7.6	1.452×10^{-50}	6.917	0.058

The critical concentration for dipole–quadrupole interactions can be calculated using the formula:

$$C_0 = \frac{3}{4\pi \times N_a \times R_0^3} \quad (4)$$

The calculated s, α, R_0 and C_0 values for the $Ce^{3+} \rightarrow Cr^{3+}$ energy transfer in CLZA:0.03Ce^{3+},0.08Cr^{3+}, CLZA:0.03Ce^{3+},0.1Cr^{3+}, and CLZA:0.03Ce^{3+},0.12Cr^{3+} are summarized in Table 5. The average value of R_0 for the $Ce^{3+} \rightarrow Cr^{3+}$ energy transfer in CLZA was 6.917 Å. This value is close to the R_0 of $Ce^{3+} \rightarrow Cr^{3+}$ in YAG, which is 6.3 Å.[37] The average value of C_0 for the $Ce^{3+} \rightarrow Cr^{3+}$ energy transfer in CLZA was 5.8%. For comparison, the C_0 for $Tm^{3+} \rightarrow Tm^{3+}$ cross relaxation in Lu_2O_3 is 1.55%, and the C_0 for the $Tm^{3+} \rightarrow Er^{3+}$ energy transfer in Lu_2O_3 is 0.12%.[38] Thus, the large C_0 value of $Ce^{3+} \rightarrow Cr^{3+}$ suggests an inefficient $Ce^{3+} \rightarrow Cr^{3+}$ energy transfer process. This conclusion seems to conflict with the high energy transfer rate shown in Fig. 7. It's important to note that C_0 only shows the property of a single Ce^{3+}–Cr^{3+} ion pair. Although the energy transfer rate between a single Ce^{3+}–Cr^{3+} pair is low, the concentration of Cr^{3+} was high. Thus the total energy transfer rate was high. Thus, concentrations of Ce^{3+} and Cr^{3+} play a key role in creating an efficient Ce^{3+}–Cr^{3+} energy transfer process.

Fig. 9 shows the excitation and diffuse reflection spectra of CLZA:xCe^{3+},0.08Cr^{3+} samples. The excitation peaks in Fig. 9a at 450 nm and 650 nm originate from Cr^{3+}. The corresponding absorption intensities of Cr^{3+} in Fig. 9b are unchanged. This is reasonable since the Cr^{3+} concentration was unchanged. The excitation peaks in Fig. 9a at 350 nm and 410 nm originate from the Ce^{3+} ion. The relative excitation intensities of Ce^{3+} increased with increasing Ce^{3+} concentration. At the same time, the absorption intensities of Ce^{3+} in Fig. 9b also increased. This was caused by a higher Ce^{3+} concentration. Thus a higher Ce^{3+} concentration is beneficial for a high absorption ability and a high energy transfer rate.

Fig. 10a shows the emission spectra of CLZA:xCe^{3+},0.08Cr^{3+} when excited by 350 nm. Since the detector of the spectrometer was insensitive to NIR light, the intensity of the Cr^{3+} emission was underestimated by about 30 times. The emission peaks at 400–650 nm originated from Ce^{3+}. The intensity of the Ce^{3+} emission increased with higher Ce^{3+} concentrations. The emission peaks at 650–900 nm belong to Cr^{3+}. When the Ce^{3+} concentration was low, the emission intensity of Cr^{3+} increased with higher Ce^{3+} concentration. This was caused by an increased energy transfer process. When the Ce^{3+} concentration was larger than 0.03, the intensity of the Cr^{3+} emission seemed to be saturated. Thus the optimized Ce^{3+} concentration is 0.03, and higher Ce^{3+} concentrations quench the Cr^{3+} luminescence. Fig. 11 shows the emission spectra of Cr^{3+} in CLZA:xCe^{3+},0.08Cr^{3+} when

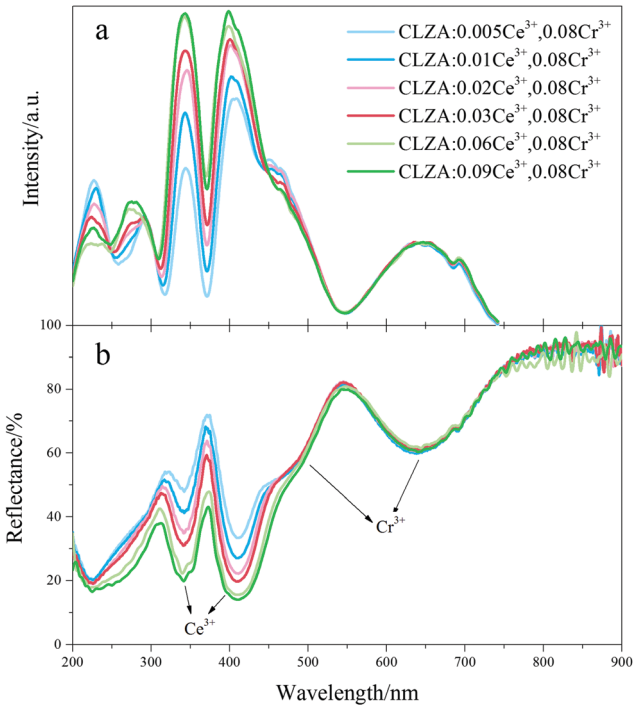

Fig. 9 (a) Excitation spectra of CLZA:xCe^{3+},0.08Cr^{3+} with different Ce^{3+} concentrations monitoring 760 nm emission. The spectra is normalized at 650 nm. (b) Diffuse reflection spectra of CLZA:xCe^{3+},0.08Cr^{3+}.

Cr^{3+} is excited alone. The emission intensities of Cr^{3+} decreased with higher Ce^{3+} concentrations. This proves that the Ce^{3+} ions introduced quenching centres for Cr^{3+}. Fig. 10b shows the emission spectra of CLZA:0.03Ce^{3+},yCr^{3+} when excited at 350 nm. The emission intensities of Ce^{3+} decreased with higher Cr^{3+} concentrations.

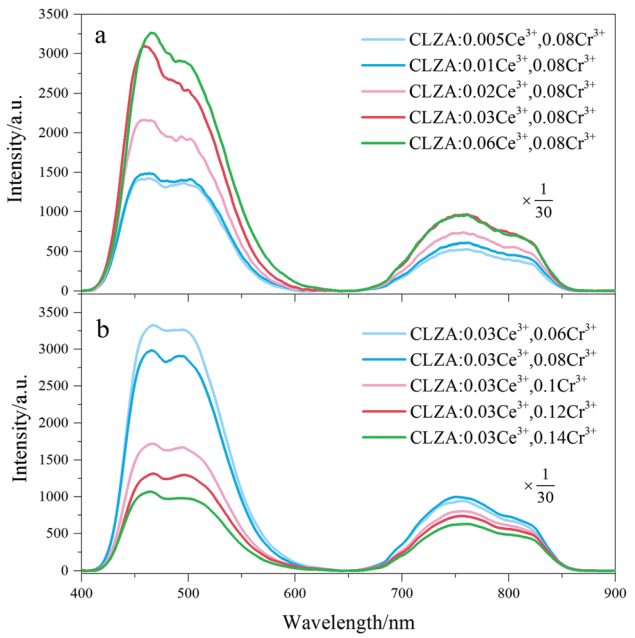

Fig. 10 (a) Emission spectra of CLZA:xCe^{3+},0.08Cr^{3+} with different Ce^{3+} concentrations when excited at 350 nm. (b) Emission spectra of CLZA:0.03Ce^{3+},yCr^{3+} with different Cr^{3+} concentrations when excited by 350 nm.

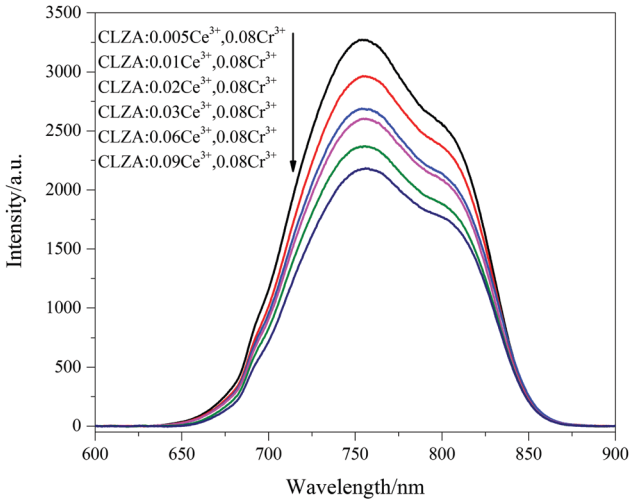

Fig. 11 Emission spectra of Cr^{3+} in CLZA:xCe^{3+},0.08Cr^{3+} samples when excited by 650 nm.

This was caused by an increased energy transfer. The emission intensity of Cr^{3+} reached a maximum when the Cr^{3+} concentration was 0.08. A higher Cr^{3+} concentration resulted in concentration quenching. Thus, CLZA:0.03Ce^{3+},0.08Cr^{3+} is the optimal combination.

Temperature stability

Fig. 12a shows a 3D plot of the temperature dependent spectrum of CLZA:0.08Cr^{3+}. The contour lines in Fig. 12a formed an "n"-shape. This indicates that the emission position and band width of CLZA:0.08Cr^{3+} were almost unchanged at different temperatures. Fig. 12b shows a 3D plot of the temperature dependent spectrum of CLZA:0.03Ce^{3+},0.08Cr^{3+}. The contour lines in Fig. 12b formed a "Ω"-shape. The band width of CLZA:0.03Ce^{3+},0.08Cr^{3+} was broadened around 200–300 K. Fig. 12d shows the temperature dependent intensities of CLZA:0.08Cr^{3+} and CLZA:0.03Ce^{3+},0.08Cr^{3+}. The intensities of CLZA:0.03Ce^{3+},0.08Cr^{3+} increased before 233.15 K. This is ascribed to the increased energy transfer from Ce^{3+} to Cr^{3+} with increasing temperature. When the temperature was higher than 353.15 K, the intensity descent process of CLZA:0.03Ce^{3+},0.08Cr^{3+} was similar to that of CLZA:0.08Cr^{3+}.

A configuration coordinate diagram is the most widely accepted tool for explaining the temperature dependence of phosphor. As shown in the top right corner of Fig. 12d, the potential energy of the luminescence center is plotted as a function of the configuration coordinate. The luminescence can be quenched through the intersection of the excited state and ground state. ΔE is the energy barrier for thermal quenching. The temperature dependence of phosphor can be described using the expression:

$$I(T) = \frac{I_0}{1 + A \cdot \exp\left(-\frac{\Delta E}{k \cdot T}\right)} \quad (5)$$

I_0 is the initial emission intensity, and ΔE is the activation energy for thermal quenching. From eqn (5), one can derive that $\ln(I_0/I - 1)$ shows a linear relationship with $1/T$. The slope is $\Delta E/k$. The plot of $\ln(I_0/I - 1)$ *vs.* $1/T$ of CLZA:0.08Cr^{3+} is

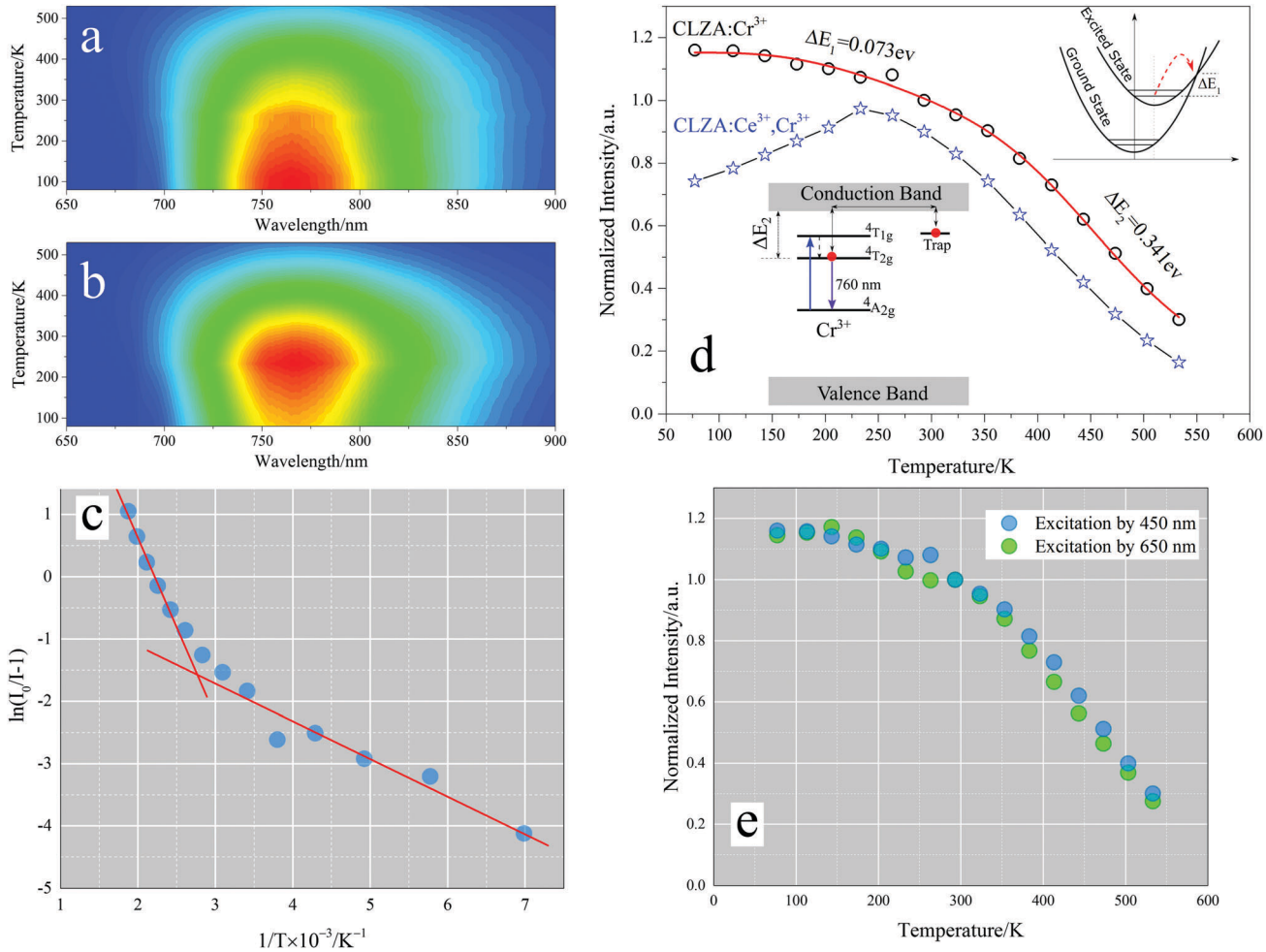

Fig. 12 3D plot of the temperature dependent spectra of CLZA:0.08Cr^{3+} when excited at 450 nm (a) and CLZA:0.03Ce^{3+},0.08Cr^{3+} when excited at 350 nm (b). (c) Plot of $\ln(I_0/I - 1)$ *vs.* $1/T$ of the temperature dependent spectrum of CLZA:0.08Cr^{3+} when excited at 450 nm. (d) Temperature dependent intensities of CLZA:0.08Cr^{3+} (black circle) and CLZA:0.03Ce^{3+},0.08Cr^{3+} (blue star). (e) Temperature dependent intensities of CLZA:0.08Cr^{3+} when excited at different wavelengths.

shown in Fig. 12c. There exist two linear processes at different temperature regions. At high temperature, the slope is much larger than that at low temperature. This indicates two thermal processes at low temperature and high temperature. The activation energy of the high temperature process is larger than that of the low temperature process, as suggested by the slope. For multi-thermal processes, the temperature dependent intensity can be expressed using the expression:[39]

$$I(T) = \frac{I_0}{1 + A_1 \cdot \exp\left(-\frac{\Delta E_1}{k \cdot T}\right) + A_2 \cdot \exp\left(-\frac{\Delta E_2}{k \cdot T}\right)} \quad (6)$$

ΔE_1 and ΔE_2 are activation energies for the two different processes. The fitting result is shown in Fig. 12d (red line). ΔE_1 equalled 0.073 eV and was associated with the low temperature process. ΔE_2 equalled 0.341 eV and was ascribed to the high temperature process. ΔE_1 should be the activation energy for thermal quenching. The value is small compared with that of other ions, for example, ΔE for Ce^{3+} in $Ca_3Sc_2Si_3O_{12}$ and $SrAlSi_4N_7$ is 0.18 eV.[40] This implies a poor thermal stability.

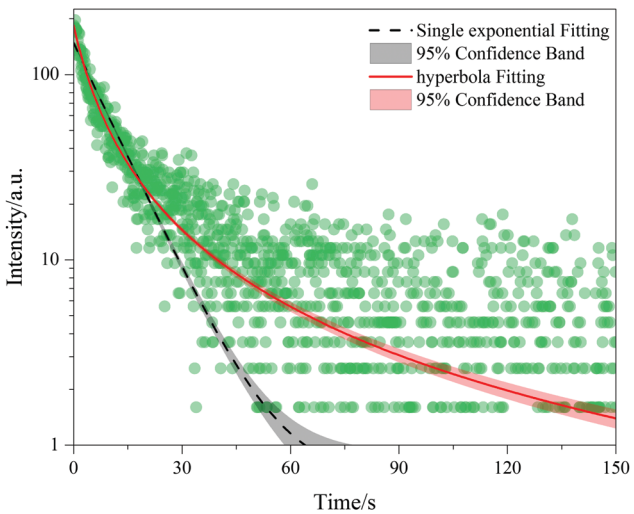

Fig. 13 Afterglow curve of CLZA:0.08Cr^{3+} monitoring at 760 nm after 450 nm excitation.

As shown in Fig. 12d, the intensity at 473.15 K decreased to 51.22% of that at room temperature.

Differently from ΔE_1, ΔE_2 is very large and should not be related to thermal quenching. ΔE_2 is the activation energy for the thermal ionization process, as shown in the left bottom of Fig. 12d. Electrons at the $^4T_{2g}$ or $^4T_{1g}$ level of Cr^{3+} may enter the conduction band *via* thermal fluctuation. The temperature dependent intensities of CLZA:0.08Cr^{3+} when excited at 450 nm ($^4T_{1g}$) and 650 nm ($^4T_{2g}$) are shown in Fig. 12e. The intensity decline processes are almost the same under 450 nm and 650 nm excitation. This indicates that ΔE_2 is the energy gap between $^4T_{2g}$ and the bottom of the conduction band. Another piece of evidence for thermal ionization is the afterglow phenomenon. Fig. 13 shows the afterglow curve of CLZA:0.08Cr^{3+} when excited at 450 nm. The lifetime of the afterglow was only 9.6 s. The afterglow curve was fitted using single exponential and hyperbola expressions separately. It is obvious that the afterglow belongs to a hyperbola type decay.

Table 6 Quantum efficiency of Cr^{3+} doped garnet phosphors

	Internal QE (%)	Absorbance (%)	External QE (%)	Ref.
CLZA:0.08Cr^{3+}	69.1	45.6	31.5	This work
CLZA:0.03Ce^{3+}	46.1	66.8	30.8	This work
CLZA:0.03Ce^{3+},0.08Cr^{3+}	36.9	68.5	25.3	This work
YGG:Cr^{3+}	46	—	—	22
GGG:Cr^{3+}	30	—	—	22
LGG:Cr^{3+}	20	—	—	22
GSGG:Cr^{3+}	21	—	—	22

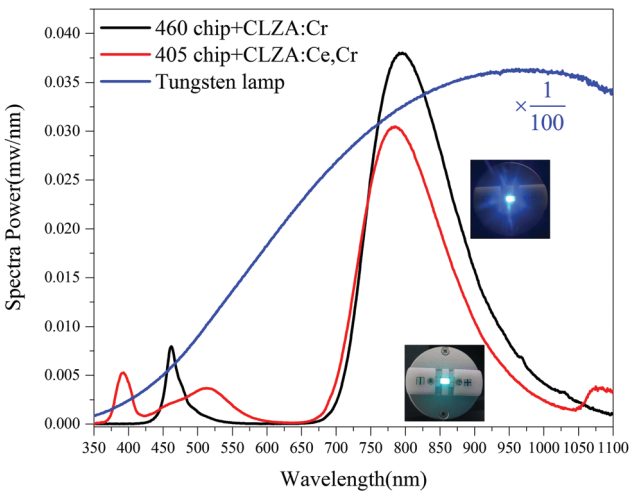

Fig. 14 Emission spectra of the tungsten lamp and the pc-LEDs made by combining a LED chip and a CLZA phosphor.

Quantum efficiency and applications

Table 6 shows the quantum efficiency of the CLZA phosphors synthesized in this paper. The internal QE of CLZA:Cr^{3+} was 69.1%, higher than that of other Cr^{3+} doped garnet phosphors. However, the absorbance of CLZA:Cr^{3+} was only 45.6%, and the external quantum efficiency was decreased to 31.5%. Even so, the external QE of CLZA:Cr^{3+} was very high among NIR phosphors. CLZA:Ce^{3+} showed an absorbance of 66.8%, much larger than that of CLZA:Cr^{3+}. In accord with the original design, co-doped Ce^{3+} increased the absorbance of CLZA:Ce^{3+},Cr^{3+} to 68.5%. However, the internal QE of CLZA:Ce^{3+},Cr^{3+} was decreased to 36.9%. This was much smaller than that of CLZA:Cr^{3+}. As mentioned in the discussion of Fig. 11, the Ce^{3+} ion introduced quenching centers for Cr^{3+}. Thanks to the improved absorbance, the external QE of CLZA:Ce^{3+},Cr^{3+} was similar to that of CLZA:Cr^{3+}.

A CLZA:0.08Cr^{3+} phosphor was combined with a 460 nm blue LED chip to form a pc-LED device. The emission spectrum of the pc-LED is shown as a black line in Fig. 14. A photo of the pc-LED device shows a blue light. This is the color of the 460 nm LED chip. The NIR emission from the CLZA:0.08Cr^{3+} phosphor is invisible to the human eye. The CLZA:0.03Ce^{3+},0.08Cr^{3+} phosphor was coated onto a 403 nm LED chip to form a pc-LED device. The emission spectrum of the device is shown as a red line in Fig. 14. The device gives off an aqua color when lit. This is the color of the Ce^{3+} luminescence in CLZA. Table 7 shows the photoelectric properties of the pc-LEDs. The photoelectric properties of the pc-LEDs were compared with those of a commercial tungsten lamp. The tungsten lamp showed higher photoelectric efficiency (22.9%) in the 350–1100 nm spectrum range. However, the photoelectric efficiency of the tungsten lamp in the 750–820 nm NIR spectrum range was only 2.9%. Most of the light energy emitted from a tungsten lamp is useless. The photoelectric efficiencies at the 750–820 nm range of the pc-LEDs with CLZA:0.08Cr^{3+} and CLZA:0.03Ce^{3+},0.08Cr^{3+} were 4.1% and 3.4% better than that of a tungsten lamp, respectively. The photoelectric efficiency of CLZA:0.03Ce^{3+},0.08Cr^{3+} was lower than that of CLZA:0.08Cr^{3+}. This is ascribed to the lower photoelectric efficiency of the 403 nm LED chip compared with the 460 nm LED chip.

Conclusions

A NIR broad-band CLZA:Cr^{3+} phosphor was synthesized in this paper. Two peaks of Cr^{3+} emission centered at 754 nm (Cr1) and 813 nm (Cr2) were observed. Cr1 originated from Cr^{3+} occupying Ca^{2+}/Lu^{3+} sites. Cr2 was attributed to Cr^{3+} occupying Zr^{4+} sites. Ce^{3+} was co-doped with Cr^{3+} in CLZA to increase the absorbance

Table 7 Photoelectric properties of the LED chip, the tungsten lamp and the pc-LEDs with CLZA phosphors

	Input electrical power (mW)	350–1100 nm optical power (mW)	350–1100 nm photoelectric efficiency (%)	750–820 nm optical power (mW)	750–820 nm photoelectric efficiency (%)
460 nm chip	60 (20 mA)	27.19	51.28	—	—
CLZA:Cr^{3+}	60 (20 mA)	6.483	8.51	2.448	4.1
403 nm chip	60 (20 mA)	18.34	30.58	—	—
CLZA:Ce^{3+},Cr^{3+}	60 (20 mA)	5.532	9.91	2.008	3.4
Tungsten lamp	7783 (1.55 A)	1782	22.90	223.6	2.9

of the phosphor. The energy transfer rates from Ce^{3+} to Cr^{3+} ranged from 74.73% to 84.11% with different Cr^{3+} concentrations. This energy transfer rate was high. However, the energy transfer between a single Ce^{3+}–Cr^{3+} pair was not efficient, as suggested by the critical concentration for the $Ce^{3+} \rightarrow Cr^{3+}$ transfer (5.8%). The high energy transfer rate was ascribed to a high concentration of Cr^{3+}. The thermal intensity dependent spectrum of CLZA:Cr^{3+} showed two thermal processes. One was the thermal quenching of CLZA:Cr^{3+} with an activation energy of 0.073 eV. The other one was the thermal ionization process with an activation energy of 0.341 eV. CLZA:Cr^{3+} showed an internal QE of 69.1%, an absorbance of 45.6%, and an external QE of 31.5%. A pc-LED device was fabricated by combining CLZA:Cr^{3+} with a 460 nm LED chip. The photoelectric efficiency in the 750–820 nm spectrum range of the pc-LED was 4.1%, superior to that of a tungsten lamp (2.9%).

Conflicts of interest

There are no conflicts to declare.

Acknowledgements

This work was partially supported by the National Key R&D Program of China (Grant No. 2016YFB0701003, 2016YFB0400605, 2017YFB0403104), the National Natural Science Foundation of China (Grant No. 51772286, 51402284 and 11604330), the Natural Science Foundation of Jilin province (Grant No. 20150520022JH and 20160520171JH), and the prior sci-tech program of innovation and entrepreneurship of oversea Chinese talent of Jilin province.

Notes and references

1 M. Ye, Z. Gao, Z. Li, Y. Yuan and T. Yue, *Food Chem.*, 2016, **190**, 701.
2 A. Guelpa, F. Marini, A. Plessis, R. Slabbert and M. Manley, *Food Control*, 2017, **73**, 1388.
3 M. Ferrari and V. Quaresima, *NeuroImage*, 2012, **63**, 921.
4 I. Afara, I. Prasadam, Z. Arabshahi, Y. Xiao and A. Oloyeda, *Sci. Rep.*, 2017, **7**, 11463.
5 N. Nagata, H. Nakanotani and C. Adachi, *Adv. Mater.*, 2017, **29**, 1604265.
6 Y. Yamanaka, H. Nakanotani, S. Hara, T. Hirohata and C. Adachi, *Appl. Phys. Express*, 2017, **10**, 074101.
7 D. Li, D. Han, S. Qu, L. Liu, P. Jing, W. Ji, X. Wang, T. Zhang and D. Shen, *Light: Sci. Appl.*, 2016, **5**, e16120.
8 C. Xie, P. You, Z. Liu, L. Li and F. Yan, *Light: Sci. Appl.*, 2017, **6**, e17023.
9 B. Nicllai, K. Beullens, E. Bobelyn, A. Peirs, W. Saeys, K. Theron and J. Lammertyn, *Postharvest Biol. Technol.*, 2007, **46**, 99.
10 S. Jones, S. Chisa, N. Chaturvedi and A. Hunhes, *Artery Res.*, 2016, **16**, 25.
11 S. Fuchi and K. Terasawa, *Phys. Status Solidi C*, 2011, **9**, 2653.
12 R. Filippo, E. Taralli and M. Rajteri, *Sensors*, 2017, **17**, 1673.
13 T. Pulli, T. Donsberg, T. Pikeonen, F. Manoocheri, P. Karha and E. Ikonen, *Light: Sci. Appl.*, 2015, **4**, e332.
14 H. Chen, R. Zhu, J. He, W. Duan, W. Hu., Y. Lu, M. Li, S. Lee, Y. Dong and S. Wu, *Light: Sci. Appl.*, 2016, **6**, e17043.
15 K. Oshima, K. Terasawa, S. Fuchi and Y. Takeda, *Phys. Status Solidi C*, 2012, **12**, 2340.
16 S. Fuchi, A. Sakano, R. Mizutani and Y. Takeda, *Appl. Phys. Express*, 2009, **2**, 032102.
17 S. Nishimura, S. Fuchi and Y. Takeda, *J. Mater. Sci.: Mater. Electron.*, 2017, **28**, 7157.
18 S. Moller, A. Katalnikovas, M. Hasse and T. Justel, *J. Lumin.*, 2016, **172**, 185.
19 S. Zhou, G. Feng, B. Wu, S. Xu and J. Qiu, *J. Phys. D: Appl. Phys.*, 2007, **40**, 2472.
20 Z. Gao, Y. Liu, J. Ren, Z. Fang, X. Lu, E. Lewis, G. Farrell, J. Yang and P. Wang, *Sci. Rep.*, 2017, **7**, 1783.
21 M. Hughes, H. Rutt, D. Hewak and R. Curry, *Appl. Phys. Lett.*, 2007, **90**, 031108.
22 A. Zabiliute, S. Butkute, A. Zukauskas, P. Vitta and A. Kareiva, *Appl. Opt.*, 2014, **53**, 907.
23 Z. Xue, X. Li, Y. Li, M. Jiang, H. Liu, S. Zeng and J. Hao, *ACS Appl. Mater. Interfaces*, 2017, **9**, 22132.
24 J. Li, J. Shi, C. Wang, P. Li, Z. Yu and H. Zhang, *Nanoscale*, 2017, **9**, 8631.
25 Y. Li, Y. Li, R. Chen, K. Sharafudeen, S. Zhou, M. Gecevicius, H. Wang, G. Dong, Y. Wu, X. Qin and J. Qiu, *NPG Asia Mater.*, 2015, **7**, e180.
26 J. Yang, Y. Liu, Y. Zhao, Z. Gong, M. Zhang, D. Yan, H. Zhu, C. Liu, C. Xu and H. Zhang, *Chem. Mater.*, 2017, **29**, 8119.
27 H. Lin, G. Bai, T. Yu, M. Tsang, Q. Zhang and J. Hao, *Adv. Opt. Mater.*, 2017, **5**, 1700227.
28 P. Dorenbos, *Phys. Rev. B: Condens. Matter Mater. Phys.*, 2000, **62**, 15640.
29 P. Dorenbos, *Phys. Rev. B: Condens. Matter Mater. Phys.*, 2000, **62**, 15650.
30 P. Dorenbos, *Phys. Rev. B: Condens. Matter Mater. Phys.*, 2001, **64**, 125117.
31 P. Dorenbos, *J. Lumin.*, 2002, **99**, 283.
32 X. Wang and Y. Wang, *J. Phys. Chem. C*, 2015, **119**, 16208.
33 X. Gong, J. Huang, Y. Chen, Y. Lin, Z. Luo and Y. Huang, *Inorg. Chem.*, 2014, **53**, 6607.
34 T. Wang, Z. Xia, Q. Xiang, S. Qin and Q. Liu, *J. Lumin.*, 2015, **166**, 106.
35 B. Struve and G. Huber, *Appl. Phys. B: Photophys. Laser Chem.*, 1985, **36**, 195.
36 N. George, A. Pell, G. Dantelle, K. Page, A. Llobet, M. Balasubramanian, G. Pintacuda, B. Chmelka and R. Seshadri, *Chem. Mater.*, 2013, **25**, 3979.
37 L. Wang, X. Zhang, Z. Hao, Y. Luo, J. Zhang and X. Wang, *J. Appl. Phys.*, 2010, **108**, 093515.
38 L. Zhang, Z. Hao, X. Zhang, G. Pan, Y. Luo, H. Wu, X. Ba and J. Zhang, *Inorg. Chem.*, 2017, **56**, 13062.
39 Q. Zhu, L. Wang, N. Hirosaki, L. Hao, X. Xu and R. Xie, *Chem. Mater.*, 2016, **28**, 4829.
40 L. Zhang, J. Zhang, X. Zhang, Z. Hao, H. Zhao and Y. Luo, *ACS Appl. Mater. Interfaces*, 2013, **5**, 12839.

